Effect of Phase Structure of MnO_2 Nanorod Catalyst on the Activity for CO Oxidation

Shuhui Liang, Fei Teng, G. Bulgan, Ruilong Zong, and Yongfa Zhu*

Department of Chemistry, Tsinghua University, Beijing 100084, P. R. China

Received: September 17, 2007; In Final Form: January 28, 2008

The α-, *β*-, *γ*-, and *δ*-MnO_2 nanorods were synthesized by the hydrothermal method. Their catalytic properties for CO oxidation were evaluated, and the effects of phase structures on the activities of the MnO_2 nanorods were investigated. The activities of the catalysts decreased in the order of α- ≈ *δ*- > *γ*- > *β*-MnO_2. The mechanism of CO oxidation over the MnO_2 nanorods was suggested as follows. The adsorbed CO was oxidized by the lattice oxygen, and the MnO_2 nanorods were partly reduced to Mn_2O_3 and Mn_3O_4. Then, Mn_2O_3 and Mn_3O_4 were oxidized to MnO_2 by gaseous oxygen. CO chemisorption, the Mn−O bond strength of the MnO_2, and the transformation of intermediate oxides Mn_2O_3 and Mn_3O_4 into MnO_2 can significantly influence the activity of the MnO_2 nanorods. The activity for CO oxidation was mainly predominated by the crystal phase and channel structure of the MnO_2 nanorods.

1. Introduction

MnO_2 is an excellent catalyst for volatile organic compounds (VOC) oxidation, and much research has been focused on its catalytic property.[1−3] MnO_2 can form many kinds of polymorphs, such as α-, *β*-, *γ*-, and *δ*-MnO_2, when the MnO_6 octahedral units are linked in different ways.[4−8] It is generally accepted that the phase structure can significantly influence the catalytic activity of MnO_2.[9,10] Recently, Wang et al. reported that a α-MnO_2 nanorod sample showed a higher activity for CO oxidation than a *β*-MnO_2 nanorod sample because α-MnO_2 can be reduced at lower temperature.[10] Besides, the different numbers of active sites and crystal plane effects explained why the nanorods showed higher activity than the corresponding nanoparticles.[11−13] The chemisorption of the reactants over the catalysts is closely related to the catalytic reaction.[14−16] However, few investigations have been done on the CO chemisorption and CO oxidation mechanism over MnO_2 nanorods. The α-, *β*-, *γ*-, and *δ*-MnO_2 oxides all formed infinite channels with different dimensions, which display novel functionalities in gas adsorption, gas diffusion, and catalytic reaction.[17−21] Therefore, it is necessary to reveal the relationship between the channel structures of MnO_2 nanorods and the catalytic activities for CO oxidation in order to investigate the mechanism and elucidate the factors dominating the catalytic properties of MnO_2 nanorods.

In this work the α-, *β*-, *γ*-, and *δ*-MnO_2 nanorods were synthesized by the hydrothermal process. The structures and catalytic performances of the MnO_2 nanorod catalysts have been revealed by TEM (transmission electron microscopy), XRD (X-ray diffraction), CO and CO_2-TPD (temperature-programming desorption), H_2-TPR (temperature-programming reduction), Raman and FT-IR, XPS (X-ray photoelectron spectroscopy), and CTL (cataluminescence). The effects of the crystal phase and channel structure of the MnO_2 nanorods on CO catalytic oxidation were investigated. The main factors that dominated the catalytic activities of the MnO_2 nanorods were elucidated, and the mechanism of CO catalytic oxidation was proposed.

* To whom correspondence should be addressed. Phone: +86-10-62783586. Fax: +86-10-62787601. E-mail: zhuyf@tsinghua.edu.cn.

2. Experimental Section

2.1. Synthesis of MnO_2 Nanorod Catalyst. In a typical synthesis of the α-MnO_2 nanorods, 0.50 g of $KMnO_4$ and 0.21 g of $MnSO_4{\cdot}H_2O$ were mixed in distilled water (32 mL) and magnetically stirred about 10 min to form a homogeneous mixture. Then, the mixture was transferred into a Teflon-lined stainless steel autoclave (40 mL) and heated at 160 °C for 12 h.[5] The product was collected, washed, and dried at 80 °C. Similarly, the *β*-MnO_2 nanorods were obtained from the reaction of $KMnO_4$ (0.28 g) and $MnSO_4{\cdot}H_2O$ (0.45 g) at 160 °C for 12 h. For the preparation of the *γ*-MnO_2 nanorods, $MnSO_4{\cdot}H_2O$ (1.35 g) and $(NH_4)_2S_2O_8$ (1.83 g) were well mixed and hydrothermally treated at 90 °C for 24 h. The *δ*-MnO_2 nanorods were obtained by the chemical oxidation of $MnSO_4{\cdot}H_2O$ (0.11 g) and $KMnO_4$ (0.6 g), which were hydrothermally heated at 240 °C for 24 h.

2.2. Characterization. The samples were characterized by XRD (Rigaku D/MAX-2500 X-ray powder diffractometer) using graphite-monochromated Cu Kα radiation ($\lambda = 0.154$ nm). A 0.02 step in 2θ/count, beam voltage of 40 kV, and beam current of 300 mA were used. The powders were packed into a glass sample holder for data collection. The BET (Brunauer−Emmett−Teller) surface areas of the catalysts were determined by N_2 adsorption at −196 °C using a Tristar 2010 chemical adsorption instrument (Micromeritics). The morphology and size of the MnO_2 samples were observed on a TEM (1200EX) instrument with an accelerating voltage of 100 kV. Raman spectra were measured at room temperature using a Jobin Yvon/Atago-Bussan T-64000 triple spectrometer. An Ar-ion laser, 514.5 nm (10 mW), and a He−Ne laser, 632.8 nm (20 mW), were used to excite the Raman spectra. Measurements were carried out under the microscope using a 90 microscopy objective, and the laser spot size was around 1−2 μm. The spectra were collected in the range of 100−900 cm^{-1} with a resolution of 2 cm^{-1}. Infrared transmission spectra were collected with a Perkin-Elmer 1600 FT-IR spectrometer at room temperature. KBr disks were mixed with the MnO_2 powder (about 1 wt %) for data collection. The spectra were recorded in the range of 450−4000 cm^{-1} with a resolution of 4 cm^{-1}. However, the FT-IR spectra were recorded on a NEXUS 670-

10.1021/jp0774995 CCC: $40.75
Published on Web 03/18/2008

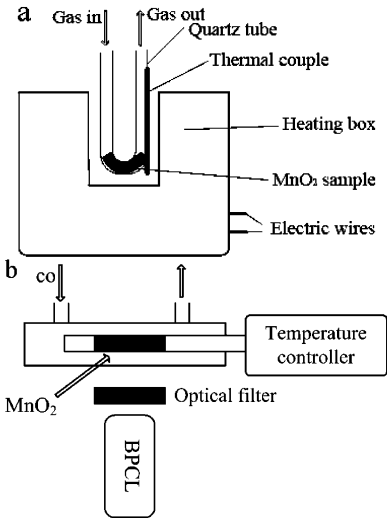

Figure 1. (a) Diagram of the catalytic reactor. (b) Diagram of the CTL system.

FT-IR instrument equipped with a smart collector and an MCT/A detector cooled by liquid N_2 at 200 °C. The MnO_2 sample (about 1 wt %) mixed with KBr was placed in a ceramic crucible. All spectra were measured in air with a resolution of 4 cm^{-1} and an accumulation of 32 scans at 200 °C. The surface composition of the catalysts was analyzed using X-ray photoelectron spectroscopy (PHI 5300 ESCA instrument). The XPS spectra were acquired using a monochromatic Al Kα X-ray source operated at 250 W. Charging effects were corrected by adjusting the binding energy of C 1s to 284.8 eV in the XPS spectra. The relative composition of each specimen was calculated from the relative XPS peak areas.

The CO-TPD (temperature-programmed desorption) measurements were performed on a conventional CO-TPD instrument. A 0.1 g amount of catalyst was located in a quartz reactor and heated at 280 °C for 2 h in He flow to remove pollutants adsorbed on the catalyst. Under flowing He gas (40 mL min^{-1}), the system was cooled naturally to room temperature. The sample was then saturated with CO at room temperature for 0.5 h. Excess adsorbate was removed by allowing the sample to remain in He flow until no significant amount of adsorbate could be detected. The temperature was then ramped to 600 °C at a linear heating rate of 10 °C min^{-1}. A mass spectrometer was used to monitor the *m*/*e* ratios at 28 (CO) and 44 (CO_2).

The H_2-TPR (temperature-programmed reduction) experiment was performed on a conventional H_2-TPR instrument. A 25 mg amount of sample was located in a quartz reactor and preheated in flowing 20% O_2 in Ar at 200 °C for 1 h. After cooling to room temperature, the sample was reduced with a 5% H_2/Ar mixture (30 mL min^{-1}) heating 10 °C min^{-1} up to 600 °C. H_2 was detected by a mass spectrometer.

2.3. Catalytic Oxidation and Cataluminescence (CTL) Measurement. Figure 1a shows the diagram of the catalytic reactor. The catalytic activities of the MnO_2 nanorods for CO oxidation were evaluated in a fixed-bed quartz tubular reactor along with a GC (gas chromatograph) detector which was with a GDX-403 GC column (1.5 m × 4 mm, 100 °C) and a FID (hydrogen flame ionization detector).[22−25] The catalyst powder (0.10 g) was placed in the "U"-shaped quartz tube. Before each run, the catalyst was flushed with air (100 mL min^{-1}) at 200 °C for 1 h in order to remove adsorbed species from the surface and then cooled to room temperature. The reaction mixture consisting of CO (the purity of CO gas is better than 99.9%) and air was introduced into the reactor, and a gas was kept at an hourly space velocity of 12 000 h^{-1}. The inlet and outlet gas compositions were analyzed by an on-line GC. The temperature range of the catalytic oxidation system was 20−800 °C with a step of 1 °C.

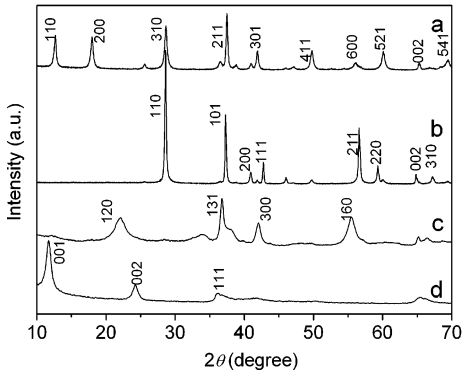

Figure 2. XRD patterns of the MnO_2 catalysts: (a) α-, (b) *β*-, (c) *γ*-, and (d) *δ*-MnO_2 nanorods. The signal intensities of the *γ*- and *δ*-MnO_2 nanorods are enlarged 10 times.

Figure 1b shows the diagram of the CTL system. A layer of catalyst with a thickness of 0.2 mm was coated on the heating tube, which was sealed into a quartz tube. A pulse of 50 mL of CO (the purity of CO gas is better than 99.9%) was injected into an air carrier that flowed through the quartz tube at a constant rate of 200 mL min^{-1}. The temperature range of the CTL system was 20−450 °C with a step of 1 °C. The CTL intensity was directly measured at a wavelength of 425 nm with a BPCL ultraweak chemiluminescence analyzer (made by the Biophysics Institute of Chinese Academy of Science in China).

3. Results

3.1. Structure and Morphology of MnO_2 Nanorods. Figure 2 shows XRD patterns of the MnO_2 nanorod catalysts (the signal intensities of the *γ*- and *δ*-MnO_2 nanorods are enlarged 10 times). Figure 2a can be well indexed to a pure tetragonal phase. The lattice constants were in good agreement with α-MnO_2 (JCPDS 44-0141). The XRD patterns in Figure 2b, c, and d corresponded to *β*-MnO_2 (JCPDS 24-0735), *γ*-MnO_2 (JCPDS 14-0644), and *δ*-MnO_2 (indexed to JCPDS 80-1098) crystal structures, respectively. The XRD patterns of the *δ*-MnO_2 nanorods gave two strong signals, which could be indexed to the [002] and [001] crystal planes. The intensities and widths of the diffraction peaks of the *γ*- and *δ*-MnO_2 nanorods were greatly lowered and widened compared with those of the α- and *β*-MnO_2 nanorods. The results showed that the *γ*- and *δ*-MnO_2 nanorods were of poor crystallinity. The surface areas, porous volumes, and crystal size of the MnO_2 nanorods are summarized in Table 1. The average sizes of the α-, *β*-, *γ*-, and *δ*-MnO_2 nanorods were 23.6, 55.4, 8.8, and 10.7 nm as calculated by the Scherrer equation. In addition, the BET surface areas of the α-, *β*-, *γ*-, and *δ*-MnO_2 nanorod catalysts were 36.5, 11.9, 61.5, and 144.4 m^2 g^{-1}, respectively.

Figure 3 shows TEM images and electron diffraction patterns of the α-, *β*-, *γ*-, and *δ*-MnO_2 samples. The diameters of the α-MnO_2 nanorods ranged between 20 and 40 nm, and the lengths ranged between 0.2 and 0.6 *μ*m. The diameters of the *β*-MnO_2 nanorods ranged between 40 and 100 nm, and the lengths ranged between 0.9 and 1.4 *μ*m. The *γ*-MnO_2 nanorods displayed uniform morphologies with diameters of approximately 20 nm and lengths of 0.1−0.4 *μ*m. The diameters of the *δ*-MnO_2 nanorods were approximately 15 nm, and the lengths were 0.5 *μ*m. Furthermore, the aspect ratios (length/diameter) of the α-, *β*-, *γ*-, and *δ*-MnO_2 nanorods were 8−15,

TABLE 1: Surface Area, Porous Volume, Crystal Size by XRD, and Aspect Ratio by TEM of the MnO_2 Nanorods

	before CO oxidation				after CO oxidation			
catalyst	SA[a] (m^2 g^{-1})	Vp[b] (mL g^{-1})	cryst size[c] (nm)	aspect radio[d]	SA[a] (m^2 g^{-1})	Vp[b] (mL g^{-1})	cryst size[c] (nm)	aspect radio[d]
α-MnO_2	36.5	0.16	23.6	8−15	32.5	0.12	31.5	10−25
β-MnO_2	11.9	0.02	55.4	15−20	11.0	0.01	64.7	10−40
γ-MnO_2	61.5	0.25	8.8	5−20	58.9	0.23	14.9	10−20
δ-MnO_2	144.4	0.42	10.7	30	139.0	0.39	12.5	50

[a] Surface area by BET method. [b] Porous volume. [c] Crystal size from XRD measurements. [d] Aspect ratio by TEM image.

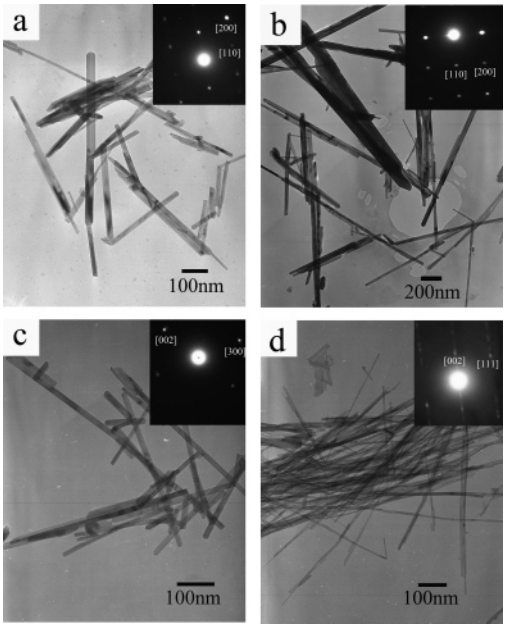

Figure 3. TEM images and electron diffraction patterns of the MnO_2 nanorods: (a) α-, (b) β-, (c) γ-, and (d) δ-MnO_2.

15−20, 5−20, and 30, respectively. The electron diffraction of a single δ-MnO_2 nanorod was weak. Only two diffraction rings could be observed from the electron diffraction patterns that could be indexed to the [002] and [001] crystal planes of the δ-MnO_2 nanorods when the electron beam focused on many nanorods (Supporting Information, Figure S1). This agreed well with the XRD result.

The control experiments were carried out to investigate the influence of hydrothermal temperature and time on formation of the MnO_2 nanorods. The sample of δ-MnO_2 nanorod was used as a probe to reveal the formation process of the MnO_2 nanorods under different hydrothermal conditions. When the reaction temperature was lower than 240 °C and the reaction time was less than 24 h, the curling lamellar (flowerlike) structures could be obtained (Supporting Information, Figure S2). It showed that the hydrothermal temperature and time had a significant influence on formation of the MnO_2 nanorods. The curling lamellar structures would grow into nanorods by a rolling mechanism.[5]

3.2. Catalysis Performance and Stability Test. The activities of the MnO_2 nanorods in CO oxidation are shown in Figure 4a, and the detail is shown in Figure 4b. CO concentration and the total flow rate maintained 2 vol. % and 70 mL min^{-1}, respectively. The catalytic activities decreased in the order of α- ≈ δ- > γ- > β-MnO_2 nanorods. The T_{10}, T_{50}, T_{90}, and T_{100} (the temperatures of CO conversion 10%, 50%, 90%, and 100%, respectively) values over the α- and δ-MnO_2 nanorods were obviously lower than those over the γ- and β-MnO_2 nanorods. Compared with the γ- or β-MnO_2 nanorods, T_{100} of the α-MnO_2 nanorods was decreased by 30 or 90 °C, respectively.

The effect of CO concentration on the activities of the MnO_2 nanorods is shown in Figure 4c. The working temperature was 140 °C mainly because CO conversions were all above 55% at the temperature, and the total flow rate of the reaction mixture maintained 70 mL min^{-1}. When CO concentration increased from 2 to 10 vol. %, CO conversions decreased by 2.9%, 12%, 27.2%, and 22.5% over the α-, δ-, γ-, and β-MnO_2 nanorods, respectively. It was clear that the effect of CO concentration on the catalytic activity of α- or δ-MnO_2 was rather small as compared with the γ- or β-MnO_2 nanorods. The effect of flow rate on CO catalytic oxidation over the MnO_2 nanorods is shown in Figure 4d. The working temperature was 140 °C, and CO concentration was 10% in volume. It could be observed that CO conversion decreased with increasing flow rate from 70 to 130 mL min^{-1}. The percentages of CO conversion decreased by 6.0%, 12.6%, 17.5%, and 20.9% over the α-, δ-, γ-, and β-MnO_2 nanorods, respectively, when the flow rate increased from 70 to 130 mL min^{-1}. The activities of the four catalysts decreased in the order of α- < δ- < γ- < β-MnO_2 with increasing flow rate. With increasing CO concentration or flow rate the activities of the α- and δ-MnO_2 nanorods decreased slightly, but those of the γ- and β-MnO_2 nanorods decreased significantly. The above results indicate that the α- and δ-MnO_2 nanorods not only had higher catalytic activities but also had higher abilities to suffer an inhibitory effect than the γ- and β-MnO_2 nanorods. This may also suggest that α- and δ-MnO_2 were not sensitive to the CO concentration and flow rate.[26,27] The conclusion could be drawn that the α- and δ-MnO_2 nanorods had higher catalytic abilities for CO oxidation than the γ-and β-MnO_2 nanorods. Tests were performed at constant space velocity but varying the amount of catalyst (0.05, 0.1, and 0.2 g) and correspondingly the flow rates (35, 70, and 140 mL min^{-1}) in order to check mass transfer affecting the kinetics. These tests showed the steadiness of CO conversions, so external mass transfer limitations did not occur.[27]

The oxidation reaction of CO was run at 140 °C for 50 h under the conditions of 2 vol. % CO and 98 vol. % air. The CO conversions at different durations of calcination are shown in Figure 4e. After running at 140 °C for 50 h, the conversions of CO over the α-, β-, γ-, and δ-MnO_2 nanorod catalysts were almost maintained. Meanwhile, the BET surface areas of the MnO_2 nanorods after a catalytic reaction for 50 h slightly decreased with respect to those before reaction (the BET surface areas of the α-, β-, γ-, and δ-MnO_2 nanorod catalysts were 30.2, 10.5, 54.8, and 135.9 m^2 g^{-1} after running at 140 °C for 50 h, respectively). This indicated that the redox features of the MnO_2 catalysts were quite stable under the CO oxidation atmosphere.

3.3. CTL Property. Figure 5 shows the CTL response to CO at different temperatures over the MnO_2 nanorods. The CTL intensities increased with increasing temperatures over the four catalysts. It was observed that the CTL intensity over the α- or δ-MnO_2 nanorods was much higher than that over the γ- or β-MnO_2 nanorods. The CTL intensities over the γ-MnO_2 nanorods were obviously higher than those over the β-MnO_2

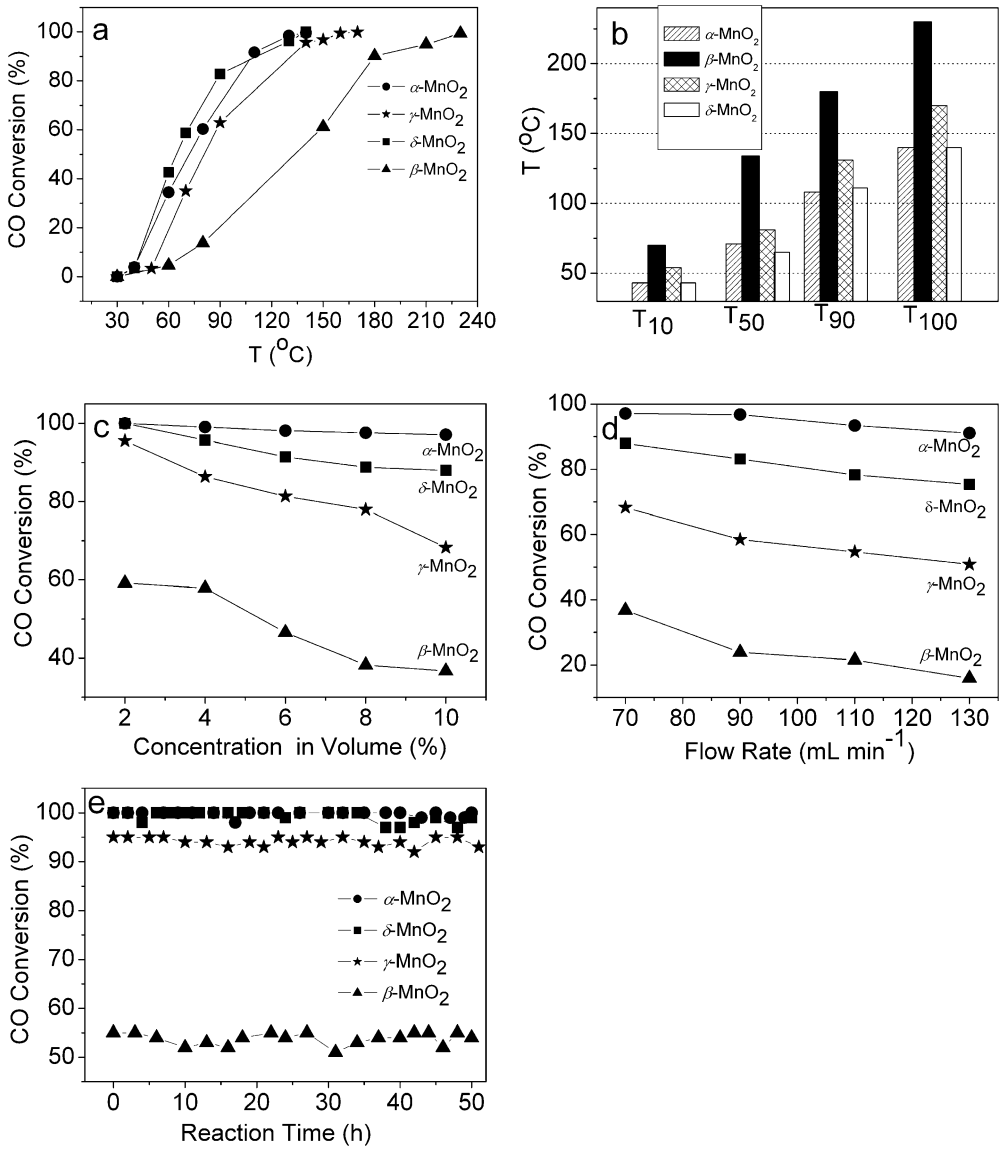

Figure 4. (a) CO oxidation activities over the MnO_2 nanorods in 2 vol. % CO and 98 vol. % air with a flow rate of 70 mL min^{-1}. (b) T_{10}, T_{50}, T_{90}, and T_{100} of the MnO_2 nanorods. T_{10}, T_{50}, T_{90}, and T_{100} are the temperatures of CO conversion 10%, 50%, 90%, and 100%, respectively. (c, d) Effects of CO concentration and flow rate on catalytic activities of the MnO_2 nanorods at 140 °C. (e) Variation of CO conversion with time over the MnO_2 nanorods in 2 vol. % CO and 98 vol. % air at 140 °C.

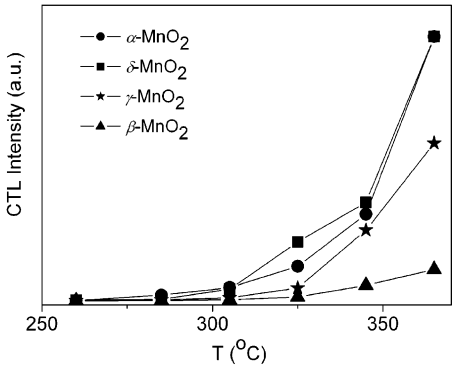

Figure 5. CTL response to CO oxidation at different temperatures over the MnO_2 nanorods.

nanorods in the whole measured temperatures. The decreasing order of CTL intensity over the MnO_2 nanorods was α- ≈ δ- > γ- > β-MnO_2, which was exactly the same as the decreasing order of activities for CO oxidation of the MnO_2 nanorods. When CO was oxidized catalytically to CO_2 on the surface of the MnO_2 nanorods, the released energy could be absorbed by some CO_2 molecules. As a result, CO_2 molecules would jump from the ground state up to the excited state. While the CO_2 molecules decayed from the excited state to the ground state, the weak CTL light would be emitted.[28] The CTL intensity was proportional to the concentration of the produced CO_2. Therefore, CTL response to CO can demonstrate the catalytic activities of the MnO_2 nanorods.[29]

3.4. CO Adsorption. CO-TPD was performed to explore CO adsorption on the MnO_2 nanorods, as shown in Figure 6. A significant portion of CO desorbed as a form of CO_2 in the process, so the total adsorption amount of CO on the catalyst was consistent with the desorption amounts of both CO_2 and CO. For the α-MnO_2 nanorods five desorption peaks of CO_2 were observed at about 100, 355, 425, 490, and 560 °C. For the β-MnO_2 nanorods two CO_2 desorption peaks appeared at about 435 and 550 °C, and their intensities were nearly same. For the γ-MnO_2 nanorods two desorption peaks of CO_2 were observed at 435 and 560 °C, which were similar to those of the β-MnO_2 sample. For the δ-MnO_2 nanorods there were two desorption peaks of CO_2 at 75 and 160 °C and a strong wide peak at 345 °C. Differences were also observed in the CO

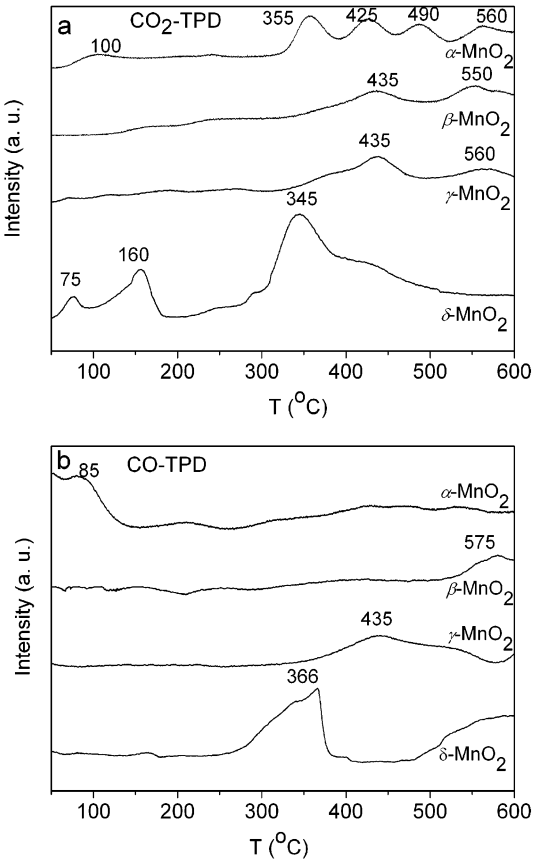

Figure 6. TPD spectra after CO adsorption over the MnO_2 nanorods: (a) TPD spectra of CO_2 and (b) TPD spectra of CO.

TABLE 2: Relative Amounts of CO and CO_2 Desorbed from the MnO_2 Nanorods (peak area per gram of catalyst)

catalyst	peak area of CO ($\times 10^4$)g^{-1}	peak area of CO_2 ($\times 10^4$)g^{-1}
α-MnO_2	38.2	8.8
β-MnO_2	16.8	3.6
γ-MnO_2	32.1	4.7
δ-MnO_2	73.7	17.9

desorption profiles in Figure 6b. The α-MnO_2 nanorods showed a broad peak at about 85 °C. For β-MnO_2 CO desorption showed a peak from 530 to 600 °C (where the experiment was stopped). The profile of CO desorption showed a broad peak from 380 to 570 °C and a tail peak from 580 to 600 °C for the γ-MnO_2 nanorods. The δ-MnO_2 nanorods showed a strong wide peak from 250 to 400 °C and a tail peak from 470 to 600 °C.

The peak areas of CO_2 or CO desorption can measure the relative desorption amounts of CO_2 or CO over the MnO_2 nanorods.[30] The integrated peak areas of CO and CO_2 are shown in Table 2. The desorption amounts of CO and CO_2 over the MnO_2 nanorods both decreased in the order of δ- > α- > γ-> β-MnO_2. Therefore, the total adsorption amount of CO also followed the order of δ- > α- > γ-> β-MnO_2 nanorods. The quantitative results showed that the total amount of CO adsorption on the δ-MnO_2 nanorods was the largest among the four samples. Moreover, the total adsorption amount of CO on the β-MnO_2 nanorods was lower compared with α-, γ-, and δ-MnO_2 nanorods.

The stabilities of the phase structures of the MnO_2 nanorods were revealed in the XRD patterns after CO-TPD, as shown in Figure 7. The α-MnO_2 maintained its phase structure very well (Figure 7a), whereas the structure of the δ-MnO_2 nanorods nearly utterly transformed to α-MnO_2 structure (Figure 7d). The

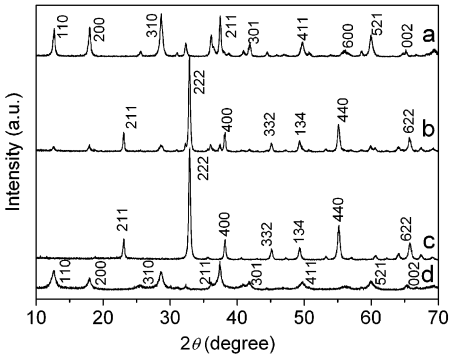

Figure 7. XRD patterns of the MnO_2 nanorods after CO-TPD experiment: (a) α-, (b) β-, (c) γ-, and (d) δ-MnO_2.

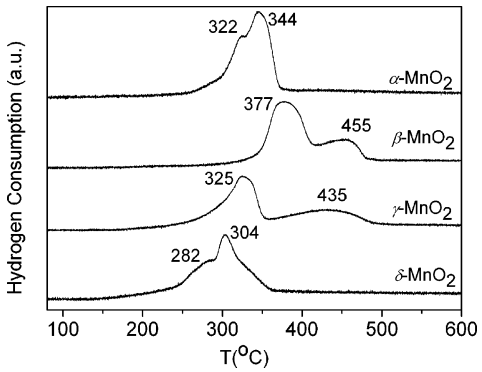

Figure 8. H_2-TPR profiles of the MnO_2 nanorods.

β- and γ-MnO_2 phases had transformed to Mn_2O_3 crystal structures (Figure 7b, c).

3.5. Reducibility. H_2-TPR profiles of the MnO_2 catalysts were performed to investigate the relative reducibility of the catalysts, as shown in Figure 8. For the β-MnO_2 nanorods, two peaks of H_2 consumption were observed at 377 and 455 °C, and the ratio of the lower temperature peak to the higher temperature peak was about 2. The TPR profile of the γ-MnO_2 nanorods was similar to that of the β-MnO_2, but two reduction peaks both shifted slightly to lower temperatures at 325 and 435 °C. The lower temperature peak should be attributed to the reduction of MnO_2 to Mn_3O_4, whereas the higher temperature peak should be attributed to the reduction of Mn_3O_4 to MnO.[10] However, the TPR profiles of the α- and δ-MnO_2 nanorods were greatly different from those of the β- and γ-MnO_2 nanorods. Two reduction peaks were observed at 322 and 344 °C for α-MnO_2 nanorods. For the δ-MnO_2 nanorods two reduction peaks were observed at 282 and 304 °C, which were similar to those of the α-MnO_2 sample. The main reduction product of the MnO_2 nanorods could be MnO, as proved by its green color after H_2-TPR experiment. The assignment of the reduction peaks was not very clear, while they may be attributed to the reduction of MnO_2 to MnO with Mn_2O_3 and Mn_3O_4 as the intermediate.[31] This finding indicated that the reduction of the four catalysts enhanced in the order of β- < γ- < α- < δ-MnO_2. The peak areas of per gram of catalyst in H_2-TPR profiles can measure relative consumption amounts of H_2.[24] The four catalysts consumed the similar amount of H_2 (peak area of H_2 was about 8.88×10^8 g^{-1}) that corresponded to reduction of MnO_2 to MnO.

3.6. Defect Structure. As a consequence of the disruption of Mn−O−Mn chains and partial leaching of Mn atom, formation of new hydroxyl groups and H_2O molecules was observed in the MnO_2 nanorods via FT-IR. The FT-IR spectra of the MnO_2 nanorods with different phase structures are shown

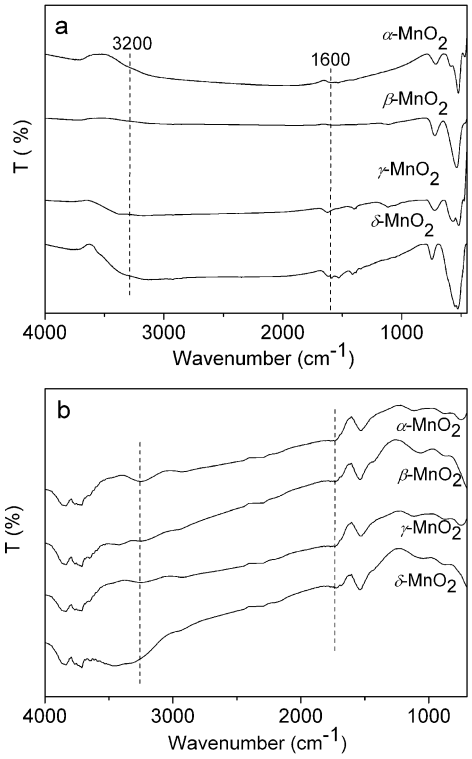

Figure 9. (a) FT-IR spectra of the MnO_2 nanorods at room temperature. (b) FT-IR spectra of the MnO_2 nanorods in air at 200 °C.

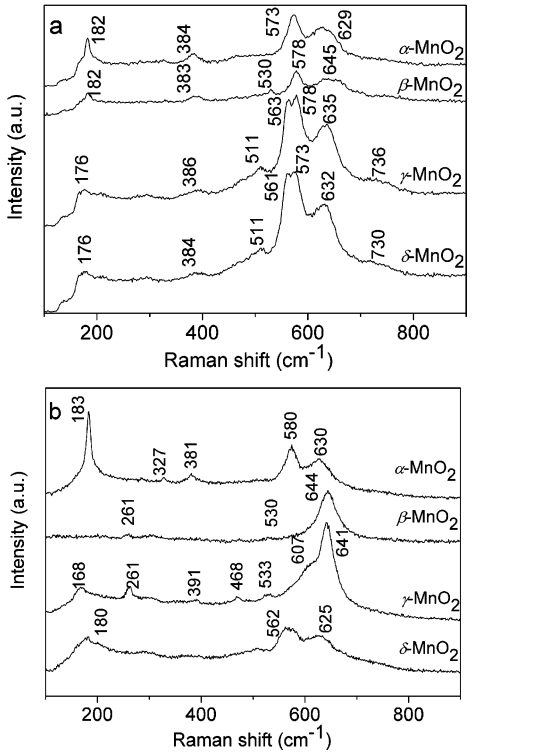

Figure 10. (a) Raman spectra of the MnO_2 nanorods using an Ar-ion laser, 514.5 nm (10 mW). (b) Raman spectra using a He−Ne laser, 632.8 nm (20 mW).

in Figure 9. The two peaks at about 520 and 720 cm^{-1} arose from the stretching vibration of the Mn−O and Mn−O−Mn bonds. The broad peak at 3200−3600 cm^{-1} could be assigned to the stretching vibration of H_2O molecule and OH^- in the lattice. The peaks of 1600 and 1200 cm^{-1} were assigned to the bending vibration of H_2O and OH^-, which implied that the hydroxyl groups existed in MnO_2 nanorods.[32−34] The results clearly indicated that the MnO_2 samples were hydroxylated. The OH^-/H_2O stretching peak of the δ-MnO_2 was the strongest among the four MnO_2 nanorods, whereas the OH^-/H_2O stretching peak of the β-MnO_2 nanorods nearly could not be distinguished. The results indicated that the amount of OH^-/H_2O on the δ-MnO_2 nanorods was the largest, and the amount of OH^-/H_2O presented on the β-MnO_2 nanorods was the smallest among the four MnO_2 nanorods. The broad peaks at 3200−3600 and 1600 cm^{-1} still existed in the MnO_2 nanorods at 200 °C, which could be assigned to vibration of the H_2O molecule and OH^- in the lattice, as shown in Figure 9b. Furthermore, the results agreed well with those at room temperature. The amount of OH^-/H_2O on the δ-MnO_2 nanorods was still the largest, and that presented on the β-MnO_2 nanorods was the smallest at 200 °C.

The Raman spectra of MnO_2 oxides showed different characters using different laser wavelength and energy.[35] Figure 10a and b shows the Raman spectra of the MnO_2 nanorods using an Ar-ion laser, 514.5 nm (10 mW), and a He−Ne laser, 632.8 nm (20 mW), respectively. The peaks across the 500−700 cm^{-1} region were attributed to the stretching mode of MnO_6 octahedra.[36,37] The peak at about 580 cm^{-1} was definitely deformation modes of Mn−O−Mn chain in the MnO_2 octahedral lattice, and the strong peak at about 630 cm^{-1} was interpreted as Mn−O stretching modes. Herein, the Raman peaks in the range of 500−700 cm^{-1} would be well discussed. The α-MnO_2 nanorods showed two strong sharp peaks at 573 and 629 cm^{-1}. The β-MnO_2 nanorods showed two strong peaks at 578 and 645 cm^{-1} along with one weak peak at 530 cm^{-1}. The γ-MnO_2 nanorods showed four peaks at 511, 563, 578, and 635 cm^{-1}. Similarly, the δ-MnO_2 nanorods also had four peaks at 511, 561, 573, and 632 cm^{-1}. The structure of the γ-MnO_2 was considered to be a random intergrowth of the ramsdellite (*R*-MnO_2) and pyrolusite (β-MnO_2) structures. The Raman profile of the γ-MnO_2 was greatly different from that of the β-MnO_2. On the basis of the results confirmed by Julien,[37] the ramsdellite (*R*-MnO_2) parts were more than pyrolusite (β-MnO_2) in the γ-MnO_2 nanorods structure.

As shown in Figure 10b the Raman spectra of the β-, γ-, and δ-MnO_2 nanorods changed greatly using the He−Ne laser, 632.8 nm (20 mW). Because of the different wavelength and intensity of the Ar-ion laser, 514.5 nm (10 mW), and He−Ne laser, 632.8 nm (20 mW), the local heating temperatures of the MnO_2 samples were obviously different. The heating stability of the α-, β-, γ-, and δ-MnO_2 nanorods were obviously different; thus, differences existed between the Raman spectra of the MnO_2 nanorods with the Ar-ion and He−Ne-ion lasers.[37,38] The β-MnO_2 nanorods only showed one strong peak at 644 cm^{-1}. The spectrum of the γ-MnO_2 showed one strong peak at 641 cm^{-1} along with a weak shoulder at 607 cm^{-1}, which was very similar to that of the β-MnO_2. The spectrum of the δ-MnO_2, showing two sharp peaks at 562 and 625 cm^{-1}, was similar to that of the α-MnO_2 nanorods, which also indicated the transformation from the δ- to the α-MnO_2 phase structure. The Raman spectra of the β- and γ-MnO_2 nanorods were more similar to that of Mn_3O_4.[38] The results indicated that the phase structures of the β- and γ-MnO_2 nanorods collapsed easily and formed Mn_3O_4 structure. These agreed well with the XRD results of the MnO_2 nanorods after CO-TPD and H_2-TPR data.

Figure 11 shows the XPS spectra of Mn 2p and O 1s in the MnO_2 nanorods. Figure 11a shows the Mn $2p_{3/2}$ peak located at 642.4 eV, which may indicate that the main manganese in all the MnO_2 nanorods were Mn^{4+}.[2] Two surface oxygen species could be clearly observed in the O 1s XPS spectra. The binding

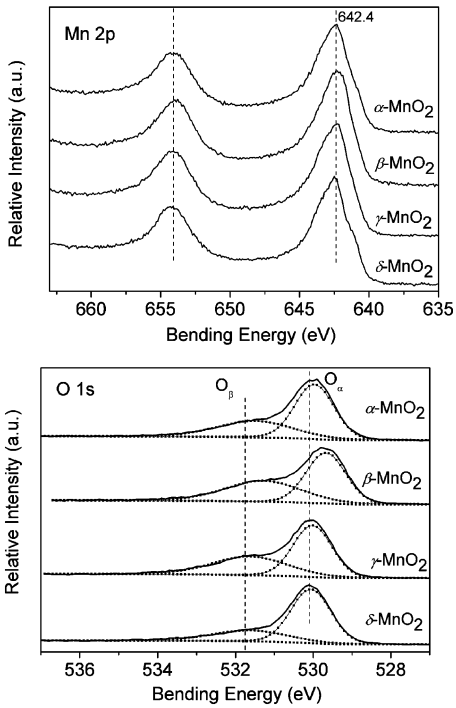

Figure 11. Mn 2p and O 1s XPS spectra of the MnO_2 nanorods.

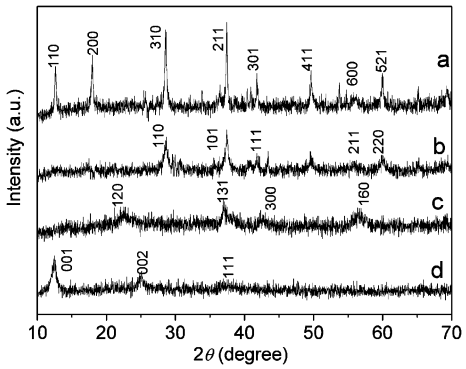

Figure 12. XRD patterns of the MnO_2 nanorods after CO catalytic oxidation: (a) α-, (b) β-, (c) γ-, and (d) δ-MnO_2. The temperatures at the end of the catalytic test were 140, 230, 170, and 140 °C over the α-, β-, γ-, and δ-MnO_2 nanorods, respectively.

energy of 529−530 eV was characteristic of the lattice oxygen (denoted as O_α), and the binding energy of 531−532 eV might be assigned to defect oxide or the surface oxygen ions with low coordination situation (denoted as O_β).[23] The corresponding concentrations of $O_\alpha(O_\alpha/O_\alpha + O_\beta)$ were 62.2%, 53.5%, 57.7%, and 78.5% for the α-, β-, γ-, and δ-MnO_2 nanorods, respectively. Obviously, the δ- and α-MnO_2 catalysts possessed richer lattice oxygen species on the surface than those of the β- and γ-MnO_2 catalysts. This phenomenon was in good accordance with the observed H_2-TPR results and catalytic activities.

3.7. Character after Catalytic Oxidation. The MnO_2 nanorod catalysts with different phase structures all maintained their nanorod morphology and phase structures after CO catalytic reaction (Supporting Information, Figure S3 and Figure 12). However, the XRD signal intensities (the signal intensities after CO catalytic oxidation decreased about 20 times) and the signal/background ratios of the four MnO_2 nanorods greatly decreased.[39] It suggested that the crystallization degrees of the four MnO_2 nanorod catalysts significantly decreased. It might be due to the fact that the manganese and oxygen ions in the MnO_2 nanorods moved off their lattice positions in the course of CO catalytic reaction. The results implied that the Mn−O bonds in the MnO_2 nanorods partly cleaved during CO oxidation.

The surface areas and porous volumes of the MnO_2 nanorods after CO catalytic reaction are also listed in Table 1. The surface areas of the α-, β-, γ-, and δ-MnO_2 nanorods were all slightly decreased by the reaction, but the BET surface areas still followed the same order δ- > γ- > α- > β-MnO_2 nanorods.

4. Discussion

4.1. Mechanism of CO Catalytic Oxidation over MnO_2 Nanorods. In order to reveal the effects of the phase structures of the MnO_2 nanorods on the catalytic activities for CO oxidation, the main factors that influence the catalytic activities of the MnO_2 nanorods are discussed. Furthermore, the mechanism of CO catalytic oxidation over the MnO_2 nanorods is investigated.

In general, the BET surface areas can greatly influence the catalytic activity. Though the BET surface area of the γ-MnO_2 nanorods (61.5 $m^2\ g^{-1}$) is much larger than that of the α-MnO_2 nanorods (36.5 $m^2\ g^{-1}$), the catalytic activity of the former is much lower compared to that of the latter. The BET surface area of the δ-MnO_2 (144.4 $m^2\ g^{-1}$) is about four times larger than that of the α-MnO_2 nanorods, whereas their catalytic activities are similar. The surface areas of the α-, β-, γ-, and δ-MnO_2 nanorods are almost stable in CO oxidation reaction. The results indicate that the catalytic activities of the MnO_2 nanorods are not significantly correlated with the BET surface areas.

On the basis of CO, CO_2-TPD, H_2-TPR, and Raman results and XRD data after CO catalytic reaction, oxidation of CO over the MnO_2 nanorod catalysts probably occurs by the following mechanism[22,40−42]

$$CO\ (ads) + 2MnO_2 \rightarrow CO_2 + Mn_2O_3 \quad (1)$$

$$CO\ (ads) + MnO_2 + Mn_2O_3 \rightarrow CO_2 + Mn_3O_4 \quad (2)$$

$$2Mn_3O_4 + O_2\ (air) \rightarrow 2MnO_2 + 2Mn_2O_3 \quad (3)$$

$$2Mn_2O_3 + O_2\ (air) \rightarrow 4MnO_2 \quad (4)$$

CO chemisorption, the Mn−O bond strength of the MnO_2 oxides, and transformation of intermediate oxides Mn_2O_3 and Mn_3O_4 into MnO_2 can significantly influence the catalytic performance of the MnO_2 nanorods.[43] The larger the amount of CO adsorption, the lower strength of the Mn−O bond and the easier transformation of intermediate oxides Mn_2O_3 and Mn_3O_4 into MnO_2 are consistent with the higher catalytic activities of the MnO_2 nanorods for CO oxidation.[44−46] On the basis of CO, CO_2-TPD data, the amount of CO adsorption on the MnO_2 nanorods with different phase structures decrease in the order of δ- > α- > γ- > β-MnO_2. The decrease in the Mn−O bond length of the MnO_2 oxide is consistent with an increase in Mn−O bond strength. The average Mn−O bond lengths of α-, β-, γ-, and δ-MnO_2 are about 1.98,[17,18] 1.88,[17,19] 1.91,[17,19] and 1.94 Å,[17] respectively. The strengths of the Mn−O bonds decrease in the order α- < δ- < γ- < β-MnO_2. On the basis of the XRD data after CO-TPD, H_2-TPR, and Raman results, the conclusion can be drawn that the transformation of intermediate oxides Mn_2O_3 and Mn_3O_4 into MnO_2 is difficult for the β- and γ-MnO_2 nanorods (Mn_2O_3 and Mn_3O_4 oxides are less active for CO catalytic oxidation[22]). The amount of CO adsorption over the α-MnO_2 nanorods is obviously smaller than

that over the δ-MnO_2 nanorods, whereas the Mn−O bond strength of the α-MnO_2 is greatly lower than that of the δ-MnO_2. Furthermore, the structure of the δ-MnO_2 nanorods can partly transform into α-MnO_2 phase structure based on the XRD results after CO-TPD, H_2-TPR, and the Raman data. Therefore, the above factors denote that the catalytic activities of the α- and δ-MnO_2 nanorods may be similar. The smaller amount of CO adsorption, the higher strength of the Mn−O bond, and the more difficult transformation of intermediate oxides Mn_2O_3 and Mn_3O_4 into MnO_2 cause the lower catalytic activities of γ- and β-MnO_2 nanorods. Compared with the β-MnO_2 nanorods, two factors are responsible for the higher catalytic activity of the γ-MnO_2 nanorods. First, the adsorption amount of CO on the γ-MnO_2 nanorods is larger than that on the β-MnO_2 nanorods. Second, the average Mn−O bond strength of the γ-MnO_2 nanorods (Mn−O bond length is 1.91 Å) is lower than that of the β-MnO_2 (Mn−O bond length is 1.88 Å).

4.2. Catalytic Activity and Phase Structure of MnO_2 Nanorods. The α-, β-, γ-, and δ-MnO_2 nanorods show different catalytic performances and CO adsorption properties. CO adsorption over the α-, β-, γ-, and δ-MnO_2 nanorods and the activities of the catalysts may correlate with their different phase structures of the MnO_2 nanorods.

The α-, β-, γ-, and δ-MnO_2 structures are all constructed from chains of MnO_6 octahedra, which link in different ways. They all form infinite channels with different dimensions. The crystal structure of α-MnO_2 consists of one-dimensional channels with relative dimensions (2×2) and (1×1) that extend along the *c* axis of a tetragonal unit cell. These channels are formed by double chains of edge-sharing MnO_6 octahedra.[17,18] The structure of β-MnO_2 has a rutile-type structure with tetragonal symmetry ($P4_2/mnm$). The MnO_6 units build up strings of edge-sharing octahedra extending along the crystallographic *c* axis. These chains are linked with neighboring chains by sharing common corners, resulting in formation of (1×1) channels in β-MnO_2 structure.[17,19] Following the work of De Wolff,[47] the structure of γ-MnO_2 is considered to be a random intergrowth of ramsdellite (2×1 channels) and pyrolusite (1×1 channels) structures. The crystal structure of ramsdellite is very similar to that of pyrolusite (β-MnO_2) except that the single chains of octahedra in pyrolusite are replaced by double chains in ramsdellite. Ramsdellite contains two kinds of oxygen atoms: one at the center of an almost equilateral triangle of cations Mn^{4+}, and the other at the apex of a trigonal pyramid of cations.[19,48] The structure of δ-MnO_2 is built up by sheets of edge-sharing MnO_6 octahedra, which are separated by layers of water molecules or hydroxide anions (OH^-). The oxygen atoms form a slightly distorted hexagonal closely packed array in the sheets of MnO. One of every six manganese sites in these layers is unoccupied, and Mn^{2+} and Mn^{3+} are considered to lie above and below these vacancies in a distorted octahedral arrangement formed by three oxygen atoms of the Mn−O layer and three hydroxide ions or water molecules of the intermediate layer. The interlayer separation of MnO sheets is approximately 7 Å.[17]

CO chemisorption is directly related to the channel structure of the MnO_2 nanorods and the content of OH^-/H_2O. Oxygen has a much higher electronegativity than hydrogen; the bonding electrons are displaced toward oxygen in the O−H bond. Therefore, the H atom in OH^-/H_2O carries a partial positive charge. It can react with the 5σ electron of the CO molecule, forming a stable connection. The δ-MnO_2 nanorods not only contain a much larger concentration of OH^-/H_2O but also have larger dimensions of channels. Therefore, the total amount of CO adsorption on the δ-MnO_2 nanorods is greatly larger than that on the α-, β-, or γ-MnO_2 nanorods. The dimensions of the channels (2×2) in the α-MnO_2 are larger compared with those of β- and γ-MnO_2. The α-MnO_2 nanorods also contain some amount OH^-/H_2O (FT-IR data). Thus, the total amount of CO adsorption on the α-MnO_2 nanorods is larger than that on the β- or γ-MnO_2 nanorods. On the basis of Raman results, the structure of the γ-MnO_2 nanorods contains more of the ramsdellite part (2×1). The part channels (2×1) of the γ-MnO_2 nanorods are slightly larger than those of β-MnO_2 (1×1). Furthermore, the OH^-/H_2O amount on the γ-MnO_2 nanorods is much larger than that on the β-MnO_2 nanorods (FT-IR results). Therefore, the γ-MnO_2 nanorods can adsorb a larger amount of CO than the β-MnO_2 nanorods. The adsorption amount of CO is the lowest over the β-MnO_2 nanorods, which may be related to the smallest dimension channel (1×1) and the lowest amount of OH^-/H_2O.

The different channel structures of the α-, β-, γ-, and δ-MnO_2 oxides are closely related to the accumulated densities of MnO_6 octahedra, as confirmed by Wang et al.[10] The channel structures with lower accumulated densities of MnO_6 octahedra can be reduced at lower temperature.[10] The channel dimensions decrease in the order α- > γ- > β-MnO_2. Similarly, the reducibility (the ability to provide lattice oxygen) also follows the same order α- > γ- > β-MnO_2. The interlayer separation of MnO sheets is approximately 7 Å, whereas the structure in the MnO sheet of δ-MnO_2 is denser than that of the α-MnO_2.[17] Therefore, the reducibility of δ-MnO_2 (release lattice oxygen) is lower than that of the α-MnO_2 nanorods.

The channel dimensions (1×1) of β-MnO_2 are too small to embed reactant (CO) in the crystal structure. Once the redox reaction takes place, the channel structure of the β-MnO_2 will be broken down.[49] Therefore, in the course of CO catalytic oxidation, the structure of the β-MnO_2 collapses easily and the transformation of intermediate oxides Mn_2O_3 and Mn_3O_4 into MnO_2 is very difficult. The structure of γ-MnO_2 is an intergrowth of ramsdellite (2×1 channels) and β-MnO_2 (1×1 channels) structures. The ramsdellite (2×1) part in the γ-MnO_2 structure is very similar to that of β-MnO_2 except that the single chains of octahedra in the β-MnO_2 are replaced by double chains. Thus, the γ-MnO_2 structure also collapses easily. The XRD data after CO-TPD and Raman results also show that the β- and γ-MnO_2 structures can be easily broken down. In conclusion, the crystal phase and channel structures of the MnO_2 nanorods are essence factors that dominate the activities of the catalysts for CO oxidation.

5. Conclusion

The α-, β-, γ-, and δ-MnO_2 nanorods were synthesized by the hydrothermal route. A mechanism of CO oxidation over the MnO_2 nanorods was proposed. The adsorbed CO reacted with the lattice oxygen, the MnO_2 nanorods were partly reduced to Mn_2O_3 and Mn_3O_4, and then intermediate oxides Mn_2O_3 and Mn_3O_4 were oxidized to MnO_2 by O_2. The catalytic activity for CO oxidation was dominated by the crystal phase and channel structure of the MnO_2 nanorods.

Acknowledgment. This work was supported by the National Basic Research Program of China (No. 2007CB613303). We are grateful to Professor Hong He of Eco-Environmental Sciences, Chinese Academy of Sciences (RCEES-CAS), for the CO-TPD and H_2-TPR data.

Supporting Information Available: Electron diffraction patterns of the δ-MnO_2 nanorods; TEM images of the δ-MnO_2

prepared at different hydrothermal conditions; TEM images of the MnO_2 nanorods after CO oxidation. This material is available free of charge via the Internet at http://pubs.acs.org.

References and Notes

(1) Lahousse, C.; Bernier, A.; Grange, P.; Delmon, B.; Papaefthimiou, P.; Ioannides, T.; Verykiosy, X. *J. Catal.* **1998**, *178*, 214.

(2) Lee, S. J.; Gavriilidis, A.; Pankhurst, Q. A.; Kyek, A.; Wagner, F. E.; Wong, P. C. L.; Yeung, K. L. *J. Catal.* **2001**, *200*, 298.

(3) Hamoudi, S.; Larachi, F.; Adnot, A.; Sayari, A. *J. Catal.* **1999**, *185*, 333.

(4) Wang, X.; Li, Y. D. *J. Am. Chem. Soc.* **2002**, *124*, 2880.

(5) Wang, X.; Li, Y. D. *Chem. Eur. J.* **2003**, *9*, 300.

(6) Subramanian, V.; Zhu, H. W.; Vajtai, R.; Ajayan, P. M.; Wei, B. Q. *J. Phys. Chem. B* **2005**, *109*, 20207.

(7) Zhou, F.; Zheng, H. G.; Zhao, X. M.; Guo, Q. X.; Ni, X. M.; Shen, T.; Tang, C. *Nanotechnology* **2005**, *16*, 2072.

(8) Zheng, D. S.; Sun, S. X.; Fan, W. L.; Yu, H. Y.; Fan, C. H.; Cao, G. X.; Yin, Z. L.; Song, X. Y. *J. Phys. Chem. B* **2005**, *109*, 16439.

(9) Cheng, F. Y.; Zhao, J. Z.; Song, W.; Li, C. S.; Ma, H.; Chen, J.; Shen, P. W. *Inorg. Chem.* **2006**, *45*, 2038.

(10) Xu, R.; Wang, X.; Wang, D. S.; Zhou, K. B.; Li, Y. D. *J. Catal.* **2006**, *237*, 426.

(11) Zhou, K. B.; Wang, X.; Sun, X. M.; Peng, Q.; Li, Y. D. *J. Catal.* **2005**, *229*, 206.

(12) Zhou, K. B.; Wang, R. P.; Xu, B. Q.; Li, Y. D. *Nanotechnology* **2006**, *17*, 3939.

(13) Wang, L.; Zhu, Y. F. *J. Phys. Chem. B* **2005**, *109*, 5118.

(14) Marthínez-Arias, A.; Fernández-García, M.; Gálvez, O.; Coronado, J. M.; Anderson, J. A.; Conesa, J. C.; Soria, J.; Munueraz, G. *J. Catal.* **2000**, *195*, 207.

(15) Hu, Y. H.; Ruckenstein, E. *J. Catal.* **1996**, *163*, 306.

(16) Craciun, R.; Nentwick, B.; Hadjiivanov, K.; Knözinger. H. *Appl. Catal. A: Gen.* **2003**, *243*, 67.

(17) Albering, J. H. *Handbook of Battery Materials, Part II Materials for Aqueous Electrolyte Batteries, 1 Structural Chemistry of Manganese Dioxide and Related Compounds*; McGraw-Hill: New York, 1999; p 85.

(18) Thackeray, M. M. *Prog. Solid State Chem.* **1997**, *25*, 1.

(19) Chabre, Y.; Pannetier, J. *Prog. Solid State Chem.* **1995**, *23*, 1.

(20) Shen, Y. F.; Zerger, R. P.; DeGuzman, R. N.; Suib, S. L.; McCurdy, L.; Potter, D. I.; O'Young, C. L. *Science* **1993**, *260*, 511.

(21) Xia, X. *Battery* **2005**, *35*, 105.

(22) Radu, C. *Catal. Lett.* **1998**, *55*, 25.

(23) Tang, X. F.; Li, Y. G.; Huang, X. M.; Xu, Y. D.; Zhu, H. Q.; Wang, J. G.; Shen, W. J. *Appl. Catal. B: Environ.* **2006**, *62*, 265.

(24) Liang, S. H.; Teng, F.; Bulgan, G.; Zhu, Y. F. *J. Phys. Chem. C* **2007**, *111*, 16742.

(25) Teng, F.; Han, W.; Liang, S. H.; Bulgan, G.; Zong, R. L.; Zhu, Y. F. *J. Catal.* **2007**, *250*, 1.

(26) Paulis, M.; Peyrard, H.; Montes, M. *J. Catal.* **2001**, *199*, 30.

(27) Cellier, C.; Ruaux, V.; Lahousse, C.; Grange, P.; Gaigneaux, E. M. *Catal. Today* **2006**, *117*, 350.

(28) Breysse, M.; Claudel, B.; Faure, L.; Guenin, M.; Williams, R. J. J.; Wolkenstein, T. *J. Catal.* **1976**, *45*, 137.

(29) Wang, X.; Na, N.; Zhang, S. C.; Wu, Y. Y.; Zhang, X. R. *J. Am. Chem. Soc.* **2007**, *129*, 6062.

(30) Xue, L.; Zhang, C. B.; He, H.; Teraoka, Y. *Appl. Catal. B: Environ.* **2007**, *75*, 157.

(31) Wang, X.; Xie, Y. C. *Catal. Lett.* **2001**, *72*, 51.

(32) Gotić, M.; Ivanda, M.; Popović, S.; Musić, S. *Mater. Sci. Eng. B* **2000**, *77*, 193.

(33) Xia, G. G.; Tong, W.; Tolentino, E. N.; Duan, N. G.; Brock, S. L.; Wang, J. Y.; Suib, S. L. *Chem. Mater.* **2001**, *13*, 1585.

(34) Nicolas-Tolentino, E.; Tian, Z. R.; Zhou, H.; Xia, G. G.; Suib, S. L. *Chem. Mater.* **1999**, *11*, 1733.

(35) Buciuman, F.; Patcas, F.; Craciun, R.; Zahn, D. R. T. *Phys. Chem. Chem. Phys.* **1999**, *1*, 185.

(36) Julien, C.; Massot, M.; Rangan, S.; Lemal, M.; Guyomard, D. *J. Raman Spectrosc.* **2002**, *33*, 223.

(37) Julien, C. M. *Solid State Ionics* **2006**, *177*, 11.

(38) Bernard, M. C.; Goff, A. H. L.; Thi, B. V.; Torresi, S. C. *J. Electrochem. Soc.* **1993**, *140*, 3065.

(39) Xia, G. G.; Yin, Y. G.; Willis, W. S.; Wang, J. Y.; Suib, S. L. *J. Catal.* **1999**, *185*, 91.

(40) Kulshreshtha, S. K.; Gadgil, M. M. *Appl. Catal. B: Environ.* **1997**, *11*, 291.

(41) Buscaa, G.; Finocchio, E.; Lorenzelli, V.; Ramis, G.; Baldi1, M. *Catal. Today* **1999**, *49*, 453.

(42) Baldi, M.; Finocchio, E.; Milella, F.; Buscaa, G. *Appl. Catal. B: Environ.* **1998**, *16*, 43.

(43) Tian, Z. R.; Xia, G. G.; Luo, J.; Suib, S. L.; Navrotsky, A. *J. Phys. Chem. B* **2000**, *104*, 5035.

(44) Torres Sanchez, R. M.; Ueda, A.; Tanaka, K.; Haruta, M. *J. Catal.* **1997**, *168*, 125.

(45) Fritsch, S.; Navrotsky, A. *J. Am. Ceram. Soc.* **1996**, *79*, 1761.

(46) Zaki, M. I.; Hasan, M. A.; Pasupulety, L.; Kumari, K. *New J. Chem.* **1998**, *22*, 875.

(47) De Wolff, P. M. *Acta Crystallogr.* **1959**, *12*, 341.

(48) Greedan, J. E.; Raju, N. P.; Wills, A. S.; Morin, C.; Shaw, S. M. *Chem. Mater.* **1998**, *10*, 3058.

(49) Yuan, Z. Z.; Zhou, Z. T.; Li, W. S. *Fine Chem.* **2004**, *21*, 91.